# Atomic force microscopy phase imaging of epitaxial graphene films

JPhys Materials

PAPER

# Atomic force microscopy phase imaging of epitaxial graphene films

**Francesco Lavini**[1,2], **Filippo Cellini**[1], **Martin Rejhon**[3], **Jan Kunc**[3], **Claire Berger**[4,5], **Walt de Heer**[4,6] and **Elisa Riedo**[1]

[1] Tandon School of Engineering, New York University, Brooklyn, NY, 11201, United States of America
[2] Department of Physics, New York University, New York, New York 10003, United States of America
[3] Institute of Physics, Charles University, Faculty of Mathematics and Physics, Prague, 121 16, Czech Republic
[4] School of Physics, Georgia Institute of Technology, Atlanta, GA, United States of America
[5] Institut Néel, CNRS-University Grenoble-Alpes, Grenoble, France
[6] TICNN, Tianjin University, Tianjin, People's Republic of China

**E-mail:** elisa.riedo@nyu.edu

**OPEN ACCESS**

**RECEIVED**
15 October 2019

**REVISED**
10 February 2020

**ACCEPTED FOR PUBLICATION**
25 February 2020

**PUBLISHED**
17 March 2020

**Keywords:** graphene, epitaxial graphene, atomic force microscopy, AFM phase imaging, friction

Supplementary material for this article is available online



## Abstract

Dynamic mode atomic force microscopy phase imaging is known to produce distinct contrast between graphene areas of different atomic thickness. But the intrinsic complexity of the processes controlling the tip motion and the phase angle shift excludes its use as an independent technique for a quantitative type of analysis. By investigating the relationship between the phase shift, the tip-surface interaction, and the thickness of the epitaxial graphene areas grown on silicon carbide, we shed light on the origin of such phase contrast, and on the complex energy dissipation processes underlying phase imaging. In particular, we study the behavior of phase shift and energy dissipation when imaging the interfacial buffer layer, single-layer, and bilayer graphene regions as a function of the tip-surface separation and the interaction forces. Finally, we compare these results with those obtained on differently-grown quasi free standing single- and bilayer graphene samples.

## Introduction

In recent years, the epitaxial growth of graphene on silicon carbide (SiC) is gaining interest thanks to its ability to provide large area, high quality graphene films that are suitable for a variety of promising technological applications [1], including electronic [2, 3], mechanical [4, 5] and optoelectronic [6, 7] systems. Epitaxial graphene (EG) continuous films are grown by high temperature sublimation of silicon atoms from SiC substrates [1, 8]. Due to the complex growth dynamics, the graphene films generally show heterogeneous surfaces, which encompasses regions with non-uniform thicknesses and properties. Given these premises, a large scientific effort is underway to investigate the fundamental properties of EG films, using and integrating non-invasive and versatile characterization techniques to rapidly gather information from the heterogeneous surface of the studied atomic thin film [9–12].

Atomic force microscopy (AFM)-based methodologies stand out for their ability to locally map the sample characteristics down to the nanometer scale, and for their operational simplicity and flexibility, which allow numerous characterization and nanomanipulation experiments to be performed *in situ* on the same sample area, and at the same time [13–15]. Among the different AFM techniques, dynamic mode AFM, and in particular AFM phase shift imaging [16–19], represents a simple technique to achieve thin films nanoscale surface characterization, free of restriction on experimental conditions and operational instrumentations. In phase imaging, contrast arises from the local changes in the energy dissipated during the oscillation of the tip over the sample surface [20]. Recording the phase shift between the excitation oscillating force and the tip response while scanning the sample has been used to map with high spatial resolution compositional information of heterogeneous surfaces [18, 21, 22]. Nevertheless, since the contributing forces related to the tip-surface energy dissipation are not trivial to distinguish and isolate, and depend on a variety of experimental factors, phase

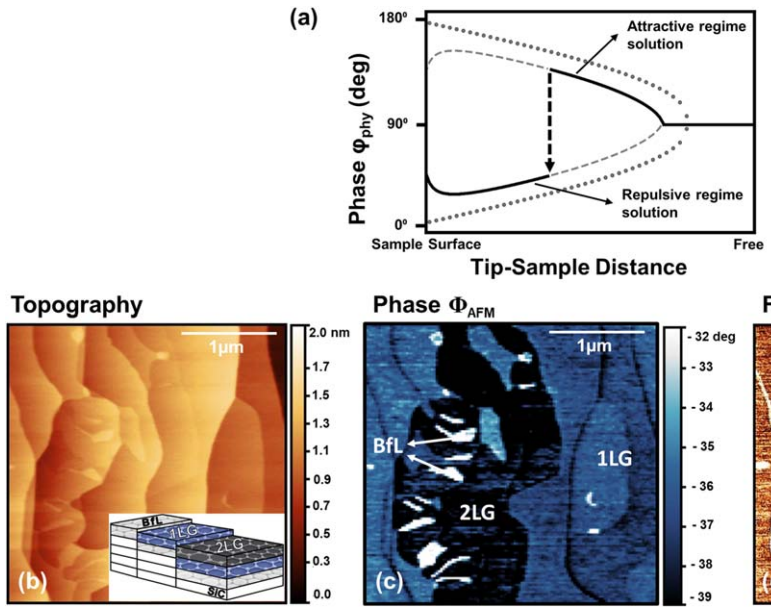


**Figure 1.** (a) Graphical representation of the phase shift angle ($\varphi_{phy}$) dependence on tip-sample separation. The image shows the two possible solutions for $\varphi_{phy}$ to equation (1), representing the two oscillation and interaction regimes the tip can experience approaching the sample surface. At resonance, the phase shift angle $\varphi_{phy}$ is exactly 90°. In the attractive regime, the phase angle $\varphi_{phy}$ increases from 90° to 180° by decreasing the tip-surface separation, while for repulsive regime the phase $\varphi_{phy}$ decreases from 90° to 0°. The arrow connecting the two solution branches represents the transition between the two interaction states. The monotonic dotted lines represent the two solutions with no inelastic terms and energy dissipation. (b) Tapping-AFM topography and the (c) corresponding phase image of the epitaxial graphene sample. (d) Contact-mode friction image collected from the same area. The image has been acquired scanning the sample with a load of 150 nN. Inset in (b): schematic representation of the epitaxial graphene film grown on SiC, highlighting the step structure of the substrate, the interface buffer layer, and the overlying single and bilayer graphene. The colors in the inset sketch in (b) have been chosen accordingly with the ones displayed in the phase map (c).

imaging is still regarded as not quantitative [23], and very few models have been provided to explain the origins of the phase contrast. The community has been aware about the capability of AFM phase imaging to obtain distinct contrast among graphene regions of different thickness, in air and at room temperature [23–26]. However, to our best knowledge, no experiments nor models have tried to explore the origin of the phase contrast in EG films. Integrated with complementary, quantitative AFM techniques, such as friction force microscopy (FFM) or Kelvin probe force microscopy, which are able to distinguish and identify the number of graphene layers on a non-homogenous surface [27, 28], AFM phase imaging can provide a complete picture of the EG properties, and shed light on how the energy dissipation mechanisms vary with the surface composition.

In this paper we explore AFM phase mapping of EG film with heterogeneous surface composition, and study the behavior of the phase shift in different regimes of oscillation and different imaging conditions, to understand the evolution of the energy dissipation mechanisms in EG, and how they relate to the thickness of the different graphene domains. Finally, we compare the dissipative processes occurring in conventional EG films with those in quasi free standing single- and bilayer graphene films (see Methods section), to explore the effect that different growth procedures and different layer structures, including the presence of the carbon interfacial buffer layer and intercalated hydrogen, may have on the tip-graphene interaction forces.

## Methods

The EG samples studied in this work are synthesized on the silicon terminated face of a 4H-SiC wafer by the confinement-controlled sublimation method [8]. Referring to the inset panel in figure 1(b), we thus consider single-layer (1LG) and bilayer (2LG) EG respectively the first and the second graphene layer overlying the interfacial buffer layer (BfL). Although this process has been extensively studied to yield large area, uniform single-layer films [29], the control of thickness distribution still remains a challenging task due to the rapid and complex evolution of the growing process. This non-uniformity allows to find graphene domains with different number of layers (BfL, 1LG and 2LG) within a small scanning area (less than 2 $\mu m^2$) and instantly compare contrast arising from phase mapping. The quasi free standing monolayer graphene (QF1LG) and quasi free standing bilayer graphene samples are prepared by hydrogen intercalation of the SiC/buffer layer interface in a buffer layer and single-layer EG sample, respectively, following the procedure indicated in [30]. Our experiments reported in figures 3 and 4, are performed on a Bruker Multimode 8 AFM, using a polycrystalline

diamond-coated silicon tip (resonance frequency $f_0 \sim 400$ kHz, spring constant $k \sim 90$ N m$^{-1}$, quality factor $Q \sim 800$). The phase imaging experiments reported in the manuscript are carried out at room temperature and in well-defined, controlled relative humidity conditions, which are specified in the description of the respective experimental set-up. The relative humidity is constantly monitored throughout the course of each experiment.

## Experimental results and discussion

### AFM phase imaging operation

The phase signal is recorded during conventional dynamic AFM mode experiments. In amplitude-modulation-AFM (AM or tapping mode AFM), the dynamics of the cantilever-tip can be modeled by a driven damped harmonic oscillator [17], whose motion is defined by its mechanical characteristics (i.e. spring constant, quality factor and resonance frequency) and by the extent of the tip-surface interaction forces. They are considered as a combination of elastic restoring and dissipative components, including long-range attractive van der Waals interactions, viscoelastic damping, adhesion and capillary forces, and short-range repulsive interactions, which are related to the material stiffness.

In tapping mode operations, the cantilever is mechanically oscillated at a fixed frequency, close to the first natural frequency of the cantilever, while being scanned over the specimen. Far from the sample surface, the cantilever oscillates freely, driven at a specific amplitude decided by the user, called free oscillation amplitude ($A_0$), and with a free phase angle $\varphi_{phy}$, usually 90°. The proximity of the tip to the sample surface influences both the nature and intensity of the interaction forces, thus causing the amplitude of the oscillation to be damped from the free $A_0$ and the phase angle to shift from its initial value. In the AM-AFM mode the amplitude of the interacting damped cantilever is used as the feedback parameter to track the topography of the sample. Since the extent of the tip-surface interaction is inversely proportional to their reciprocal distance, by decreasing the oscillation amplitude set-point ($A_{sp}$, namely the amplitude at which the cantilever is set to oscillate), normalized to the free oscillation amplitude ($A_{sp}/A_0$), it is possible to approach the tip to the sample surface. On the other hand, the shift of the phase angle $\varphi_{phy}$ is directly related to the energy dissipation ($E_{dis}$) associated with inelastic tip-surface interactions—see equation (1)—as described below [18]:

$$\sin(\varphi_{phy}) = \frac{f}{f_0}\frac{A_{sp}}{A_0} + \frac{QE_{dis}}{\pi k A_{sp} A_0}, \tag{1}$$

where $k$ is the spring constant of the cantilever, and $Q$ the quality factor. Usually the oscillation frequency $f$ is set equal to the resonance frequency $f_0$. Therefore, the phase imaging contrast arises from local variations of the tip-surface energy dissipation, thus revealing features beyond topography and inferring information about the chemical/mechanical/electrical heterogeneity of a surface. The intrinsic nonlinear character of the tip motion in AM-AFM and the participation of attractive and repulsive interactions give rise to the coexistence of two stable oscillation states, both allowed solutions for equation (1), and represented in figure 1(a) by the solid lines. The two possible oscillation regimes are distinguished by the prevalence of specific interacting forces and dissipative processes. The first branch, where the phase angle $\varphi_{phy}$ shifts from 90° up to 180°, corresponds to the attractive regime, where energy dissipation is dominated by long-range, attractive forces. The other solution corresponds to the repulsive regime. Here the phase angle $\varphi_{phy}$ decreases from 90° to 0°, and the tip-surface interaction is characterized by short-range, repulsive forces. The dotted lines in figure 1(a) represent the phase angle solutions in the absence of dissipative process: the larger the dissipative phenomena perturbing the tip oscillation, the bigger the deviation from the linear, conservative solutions [31, 32]. While introducing AFM phase mapping, one clarification is due: whereas the phase angle of the oscillating tip $\varphi_{phy}$ has a sinusoidal dependence on the tip-surface dissipation—equation (1)—and varies between 0° and 180°, being centered at 90° for free oscillation, the phase angle $\Phi_{AFM}$ extracted during AFM phase imaging is measured relatively to the free oscillation, and represents the shift from 90°. We can thus relate the two angles accordingly:

$$\Phi_{AFM} = 90° - \varphi_{phy}. \tag{2}$$

Therefore, $\Phi_{AFM}$ angle varies between 0° and −90° in the attractive regime, and between 0° and +90° in the repulsive regime.

Figure 1(b) displays a tapping-mode AFM image of the surface topography of the EG film taken simultaneously with the corresponding phase shift ($\Phi_{AFM}$) image, see figure 1(c). The same surface area is also imaged by contact mode AFM to acquire a friction map, see figure 1(d). In the tapping-AFM topography image of figure 1(b) it is possible to recognize the terraces typical of EG films, which originate from the annealing of SiC, with widths spanning from hundreds of nanometers to few micrometers. It is very difficult to discern the number of graphene layers from the topographical image, since variations in the height profile do not necessarily follow the effective changes in graphene thickness. This is due to two main reasons: first because additional graphene layers grow underneath the first one following the sublimation and out-diffusion of Si [33]—i.e. lower

height may indicate a larger number of layers—and second because of the intrinsic step structure of the SiC substrate. On the other hand, phase imaging of the same area in figure 1(c) provides a very different scenario, where some terraces with a clear different height in the topographical image show no contrast in the phase image. Furthermore, it is possible to observe new features with significant contrast and three different populations of phase values appearing in the phase image. We argue that these features represent different graphene domains, with a specific number of graphene layers. Raman spectroscopy performed on this EG sample shows that it is composed of mainly single-layer graphene with a minor presence of regions with $\pm 1$ graphene layers, i.e. BfL and 2LG, as suggested by the width of the 2D peak of the Raman spectra (see supplementary material figure S1 is available online at stacks.iop.org/JPMATER/3/024005/mmedia). In view of the abundance of data available in literature about the relationship between friction force and number of layers in EG films [28, 34, 35], we perform FFM in the same region displayed in figures 1(b) and (c), in order to comprehend the distribution of the number of graphene layers and relate it to the phase contrast. Friction images are acquired by simply switching from tapping to contact-mode AFM during the same set of experiments and using the same tip. The friction force map displayed in figure 1(d) shows the same features observed in the phase image, indicating the presence of three populations of friction values, that spatially correspond to those of the phase image. Following the results reported in literature [28], we can assign the exact number of layers to each population of friction values. In particular, we identify regions with high friction (average value of around 12 nN) to the buffer layer, the population with mid friction (average value: 1.35 nN) to 1LG, and the population with lower friction (average value: 0.8 nN) to 2LG. In fact, friction forces on 2LG regions are well known to be smaller than those measured on 1LG, and both these regions exhibit much lower friction compared to the buffer layer. The $1.7 \pm 0.1$ ratio between the 1LG and 2LG lateral forces is in good agreement with data available in literature [28], as well as the factor of 10 found between friction forces on 1LG and BfL [28]. Considering the exact spatial matching between domains in figures 1(c) and (d), we can assign a specific number of layers to the phase image regions of different contrast, as labeled in figure 1(c). Considering that phase imaging does not have any specific restrictions in terms of experimental conditions and operational instrumentations, pairing phase imaging with other quantitative AFM techniques (as FFM), could result useful and versatile in executing a variety of AFM measurements. For example, after determining the distribution of the number of graphene layers on the surface via FFM, it is possible to use phase imaging to promptly locate different graphene domains and perform targeted, *in situ* mechanical/indentation experiments [36] (possible using the same diamond-coated tip used for acquiring phase and FFM maps) and extract data selectively, without the need to change cantilever or surface location between different measurements (see figure S2 in the supplementary material).

Despite being able to distinguish regions of the film surface with different atomic thickness, phase imaging has been disregarded so far as a quantitative method to assess the exact number of atomic graphene layers in EG [23]. The tip-surface interaction forces, regulating the energy dissipation processes that cause the phase contrast to emerge, and the coexistence and transition between the two oscillating states depend on several and disparate factors, including initial experimental conditions (e.g. the tip-sample rest separation, the driving force, the driving frequency and its deviation from the cantilever natural frequency, the environmental relative humidity, the temperature) and operational parameters (e.g. the free oscillation amplitude $A_0$, and the cantilever specifications $k$, $Q$, $f_0$, among the others), together with the sample properties (e.g. elastic modulus, hydrophilicity) [37, 38]. Furthermore, modulating the amplitude of cantilever oscillation, $A_{sp}$, during the tapping mode imaging gives access to different oscillating regimes. According to the dominating interaction forces, graphene surface domains show different properties and responses. Consequently the displayed phase values and contrast vary with the experienced oscillation regime and the occurring conditions [19], making phase imaging additionally complicated to reproduce. Comparing the phase values obtained during phase imaging, $\Phi_{AFM,}$ as displayed in figures 2(a) and (b), acquired on the same region of the EG sample first at amplitude ratio $A_{sp}/A_0 = 0.9$ and then at $A_{sp}/A_0 = 0.5$, respectively, we can observe a variation in the phase contrast between 1LG and 2LG domains. Whereas for high amplitude ratio no significant phase difference is discernible among graphene domains, the appearance of phase contrast while lowering amplitude ratios—recalling the relationship reported in equation (1)—suggests alterations of both the tip-surface energy dissipation mechanisms, and the response of the two domains to the interaction forces. This shows the difficulty related to the use of phase imaging as an independent quantitative technique for the identification of graphene domains of different thickness. But it opens up to interesting questions regarding the evolution of energy dissipation mechanisms in different oscillating conditions and how these interactions vary with surface morphology.

**Origin of energy dissipation**

To further understand the relationship between phase angle and dissipative processes, and to obtain a more quantitative meaning of the phase values, as well as to explore their reproducibility, we record the variations of

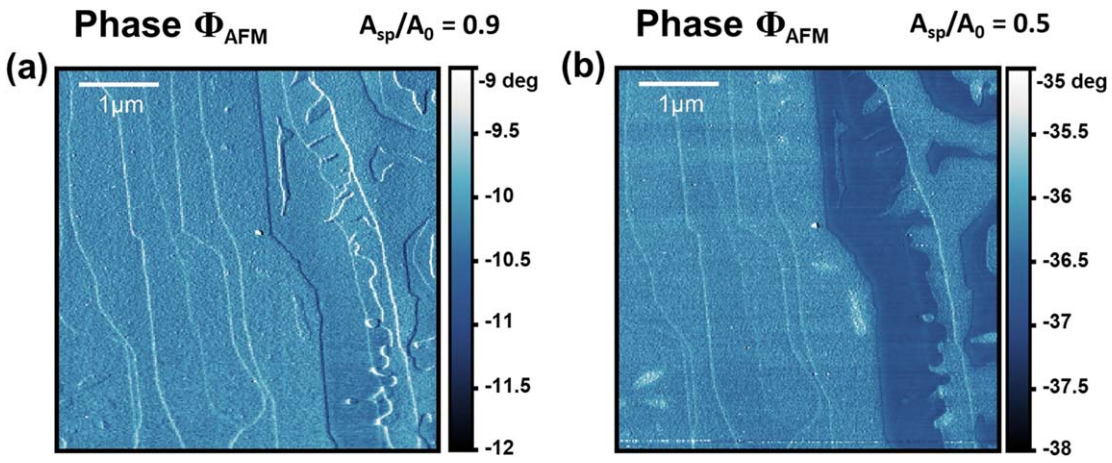


**Figure 2.** (a) and (b) show phase images ($\Phi_{AFM}$) of the epitaxial graphene sample obtained for free oscillation amplitude $A_0 = 17$ nm, and amplitude oscillation ratio $A_{sp}/A_0 = 0.9$ and $A_{sp}/A_0 = 0.5$, respectively. Phase shift angle ($\Phi_{AFM}$) values extracted are negative for both (a) and (b), and thus tip motion lies in the attractive regime, where $\varphi_{phy}$ values ranges from 90° to 180°.

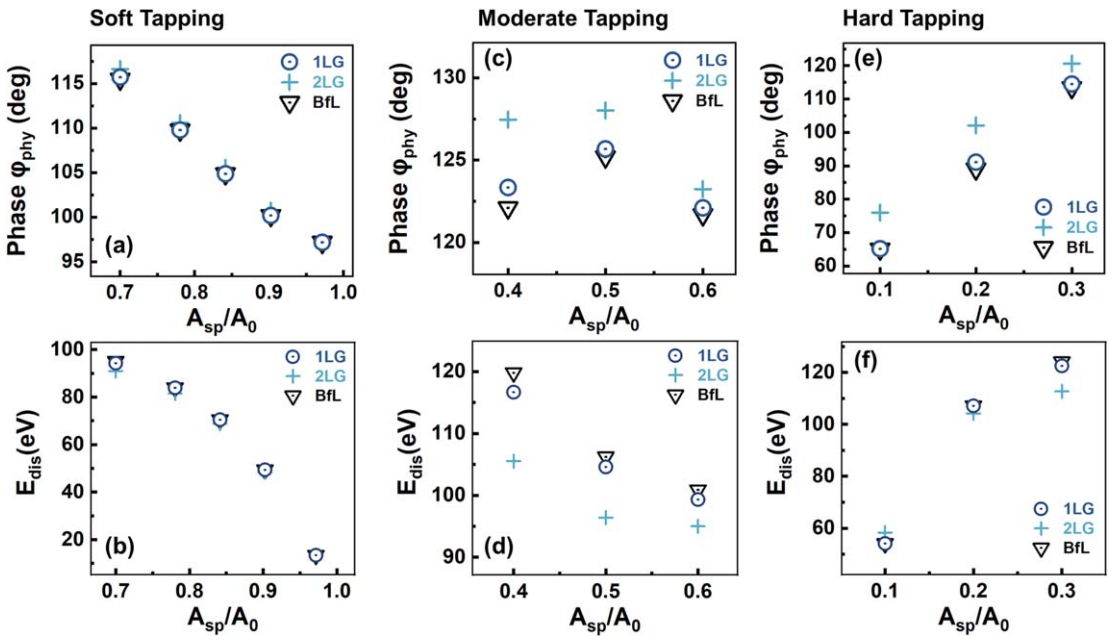


**Figure 3.** (a)–(c)–(e) Phase shift angle ($\varphi_{phy}$) variation for BfL, 1LG and 2LG, as a function of the amplitude set-point ($A_{sp}$) reduction, normalized to the free oscillation amplitude ($A_0$). Decreasing of the $A_{sp}$ corresponds to a tip-surface separation reduction. Experiment has been performed with the polycrystalline diamond-coated silicon tip, at relative humidity RH ~ 30%, with free oscillation amplitude $A_0 = 17$ nm. (b), (d)–(f) Tip-surface energy dissipation ($E_{dis}$) dependence on decreasing $A_{sp}/A_0$, corresponding to phase angles in (a)–(c)–(e) and calculated for the three graphene domains BfL, 1LG and 2LG from equation (1). In order to visually highlight the differences among phase angle values, the three oscillation regimes have been isolated: soft tapping (a)-(b), moderate tapping (c)-(d) and hard tapping (e)–(f). The reconstructed entire curves are available in figure S4 of the supplementary material.

the phase angle as a function of the tip-sample separation (namely $A_{sp}/A_0$) for BfL, 1LG and 2LG domains of the EG sample. The experiment is carried out using a polycrystalline diamond-coated silicon tip (see Methods for tip specifications), at a relative humidity of RH ~30% (constantly monitored during the experiment), with a free oscillation amplitude $A_0 = 17$ nm (details of the calibration of the free amplitude can be find in figure S3 of the supplementary material). Results are displayed in the top row of figures 3(a)–(c)–(e). We can see that the phase angle measured at moderate and soft tapping ($A_{sp}/A_0 = 0.4 - 1.0$) show values above 90°, suggesting that the tip is operating primarily in the attractive regime, which seems reasonable given that the contribution of attractive forces is more noticeable for small free amplitudes and stiff materials [38]. However, it is important to stress that, to an extent related to the initial $A_0$, during each oscillation cycle the tip feels the relative influence of both long- and short-range forces, whose intensities and contributions to the energy dissipation and phase angle vary with the tip-surface separation, and in general the dynamics of oscillations mirrors a combination of both

the interaction states. Using equation (1), from the phase angle values presented in figures 3(a)–(c)–(e) it is possible to derive the energy dissipated ($E_{dis}$) by the tip-surface interactions, and its behavior as a function of the amplitude ratio is reported in the bottom row of figures 3(b)–(d)–(f). For visual ease, the entire two graphs ($\varphi_{phy}$ versus $A_{sp}/A_0$ and $E_{dis}$ versus $A_{sp}/A_0$) have been reconstructed and reported in one single figure, displayed in figure S4 of the supplementary material.

*Long-range regime—soft tapping*

Long-range dissipative processes do not imply mechanical contact, are defined by attractive interfacial van der Waals interaction forces, and are usually derived by the non-retarded van der Waals energy and the Hamaker approach [38, 39]. In this soft tapping regime ($A_{sp}/A_0 > 0.7$), the energy dissipation is proportional to the Hamaker constant ($H$) of the material, and proportional to the inverse of the tip-sample distance, according to the following [39]

$$E_{dis} = \frac{HR}{4}\left(\frac{1}{d_1} - \frac{1}{d_2}\right), \tag{3}$$

where $R$ is the tip radius and $d_1$ and $d_2$ are the closest and the farthest tip-surface separation during the oscillation cycle. In particular, in this regime, we observe that the energy dissipated by the three graphene domains increases monotonically with the decrease of the amplitude ratio $A_{sp}/A_0$, as both $d_1$ and $d_2$ decreases while the tip approaches the sample surface, but there is no noticeable difference among their respective phase values or $E_{dis}$, as shown in figures 3(a) and (b), respectively. It is well known that for single and bilayer graphene, surface forces are heavily influenced by the underlying substrate [40]. Therefore, the Hamaker coefficient and the surface energy sensed by the oscillating tip are mainly due to the SiC. The highly hydrophilic character of the SiC substrate, together with the wetting transparency of extremely thin graphene, may explain the absence of appreciable differences in the dissipated energy for BfL, 1LG and 2LG in the long-range regime, as the tip mostly senses the properties of the substrate. In addition, more hydrophilic substrates, as SiC or $SiO_2$, have a more pronounced effect even for thicker graphene films [40].

*Short-range regime—moderate tapping*

When the tip amplitude is further decreased and it enters a more short-range regime, i.e. $A_{sp}/A_0 < 0.7$, we observe the emergence of a sensible difference between the values of phase angle—see figure 3(c)—and $E_{dis}$ for the different number of layers, with BfL and 1LG showing higher dissipation than 2LG, as shown in figure 3(d). By decreasing the tip-surface separation, short-range attractive forces, like adhesion and capillary forces, become predominant, and the energy dissipation is mostly due to the presence of adhesion hysteresis [39]. Interacting forces in this regime can be calculated by the Derjaguin–Muller–Toporov model, and the total energy dissipation is directly proportional to both surface energy hysteresis and sample deformation, according to the following [20]:

$$E_{dis} = 4\pi R\delta\Delta\gamma. \tag{4}$$

Here, $\delta$ is the sample deformation and $\Delta\gamma$ is the difference in the surface energy between the approaching and retracting curves, indicative of the adhesion hysteresis. Since in this phase the contact time is minimal, the contribution of the sample deformation to the total energy dissipated is negligible compared to the surface adhesion hysteresis. Indeed, the energy dissipation is mostly related to adhesion effects, and the observed $E_{dis}$ (BfL) $> E_{dis}$ (1L) $> E_{dis}$ (2L) is likely due to the wettability of the different domains, as their hydrophilicity follows the same trend BfL $>$ 1LG $>$ 2LG [41, 42]. Measurements obtained on thicker (>2LG) domains seem to corroborate this picture (for further details, see figure S5 in the supplementary material). We said that in this regime the energy dissipated during the oscillation cycle is proportional to the difference between the approach and retraction surface energies, which is defined by the area enclosed by the approach and retraction force curves. Initially, $E_{dis}$ continues to increase with decreasing amplitude ratio, as adhesive interactions increase approaching the surface. However, at a certain distance, a reduction of the tip-surface separation, and of the oscillation amplitude $A_{sp}$, entails also a reduction of the force–distance area enclosed by the approaching and retraction curves, which again represents the adhesion hysteresis loop. Consequently, these competing effects slow down $E_{dis}$ increasing rate, resulting in a flattening of the $E_{dis}$ curve, and eventually causing an inversion of $E_{dis}$ dependence on amplitude ratio, with $E_{dis}$ decreasing with decreasing $A_{sp}$, as observed in figure 3(f) and explained in the following section.

*Short-range regime—hard tapping*

For hard tapping ($A_{sp} < 0.3$) the dynamics of the oscillating tip enters the repulsive regime, which involves a significant mechanical hard contact time between the tip and the sample. Here, the phase $\varphi_{phy}$ approaches values below 90°, as shown in figure 3(e). The sudden transition observed between the two regimes is typical of stiff materials and small $A_0$ [38]. It is usually discouraged to work under conditions close to the attractive-repulsive

transition, as it is characterized by unstable tip motion and unstable phase values (for further details, see figure S6 of the supplementary material). For this very low tip-surface separation, contact time represents an important percentage of the total period of oscillation, and surface indentation is not negligible anymore. As displayed in figure 3(f), we consequently see an inversion of the energy dissipated by 1LG and 2LG, which is now higher for the latter, resulting from the effect of a higher indentation depth. This data is in agreement with nano-indentation measurements performed on EG [12] that proved higher contact stiffness for 1LG compared to 2LG. As the tip oscillates in hard tapping conditions, together with the transition to the repulsive regime we observe a drop in the dissipated energy. In fact, the non-conservative contribution from adhesion interaction is now considerably reduced (due to small approach and retraction force loop), and we also have the emergence of elastic, conservative effects.

In order to corroborate the proposed model, for which phase contrast in the attractive regime arises in the three graphene domains largely because of their different hydrophilicity character, and to monitor the effect of environmental humidity on phase shift and energy dissipation, we performed a comparative experiment recording phase angle $\varphi_{phy}$ as a function of the amplitude ratio $A_{sp}/A_0$ in two different controlled humidity conditions, namely moderate relative humidity conditions (RH $\sim$ 25%) and dry conditions (RH $<$ 5%). The two resulting graphs, together with the experimental details, are available in the supplementary material (see figure S7). While the data retrieved from the experiment in humid conditions mirror those presented in figure 3, we observe some differences in the results obtained in dry conditions. Here, the phase shift $\varphi_{phy}$ monotonically increases towards 180°—see figure S7(a). This behavior is typical of interactions with no or reduced non-conservative dissipative processes, and there is no transition to a short-range adhesive, attractive regime for moderate tapping. Moreover, in this condition no significant difference is noticeable among phase values of 1LG, 2LG and BfL for any amplitude ratio, suggesting the predominance of long-range interfacial interactions, as also observed in figure 3 only for high $A_{sp}/A_0$ ratios. Considering the reduced amount of water present on the sample surface in a dry environment, this picture seems to corroborate the idea that differences in phase angles and energy dissipation among the three graphene domains emerge in the attractive regime due to adhesion hysteresis. And that adhesion hysteresis contributes to the greatest extent to the energy dissipated in the attractive regime, as confirmed also by the higher $E_{dis}$ values for the humid experiment compared to the dry experiment—figure S7(b).

**Quasi free standing graphene**

To further explore the mechanism underlying energy dissipation in EG and the role of atomic structure, we compare the results obtained on the EG sample to those found in quasi free standing single—(QF1LG) and bilayer (QF2LG) graphene samples, where the buffer layer has been converted to free standing graphene by hydrogen intercalation (see Methods section). In particular, we recall that QF1LG is obtained by hydrogen intercalation at the buffer layer-SiC interface, and is equivalent to the BfL in terms of atomic thickness, while QF2LG is obtained from single-layer EG, and has therefore equivalent thickness to 1LG. Topography and phase imaging maps sampled from QF1LG and QF2LG are available in the supplementary material (see figure S9). The quasi free standing samples are examined immediately after the EG sample, using the exact same parameters employed in the experiment shown in figure 3. Figures 4(a) and (b) show respectively the variation of the phase angle $\varphi_{phy}$ and the energy dissipated $E_{dis}$, recorded while decreasing the $A_{sp}/A_0$ ratio, for the three samples measured. In the long-range attractive force regime ($A_{sp}/A_0 > 0.7$) we can observe no substantial difference in the behavior of the epitaxial and quasi free standing samples. This seems to confirm the explanation presented in the previous paragraph for the long range dissipative processes in EG, and extend it to the intercalated samples. Since all the samples share similar $E_{dis}$ values, long range tip-sample energy dissipation does not see dependence on graphene atomic thickness, and it is mostly affected by substrate interactions. Entering the short-range attractive regime ($A_{sp}/A_0 < 0.7$) the QF2LG follows the behavior of the equivalent epitaxial 1LG, suggesting that the screening effects underlying the increasing hydrophobicity with increasing number of layers [41] are not influenced by the SiC-graphene interface configuration and the presence of intercalated hydrogen, but is only dependent on the thickness, after the first carbon atomic layer. In fact, the wetting transparency responsible for the comparable wettability behavior between BfL and the substrate is observable only for the first carbon layer [41] and explains the higher energy dissipation of BfL, but it seems not to apply to QF1LG, as it shows substantially lower $E_{dis}$ values. Differently from thicker domains, the macroscopic wettability in the first carbon layer is influenced by both local substrate-carbon and carbon–water interfaces, and controlled in the buffer layer by the covalent character of the epitaxial bonding with SiC [43]. The absence of this type of interaction with the substrate, and the presence of defective intercalated hydrogen may explain the reduced adhesion hysteresis energy dissipation in QF1LG. By further decreasing the tip-sample separation and entering the hard-tapping regime, we start to observe scratching of the tip on the surface of the quasi free standing samples (respectively at $A_{sp}/A_0 < 0.3$ for QF1LG and $< 0.5$ for QF2LG), making it impossible to extract clear $\varphi_{phy}$ values. This is

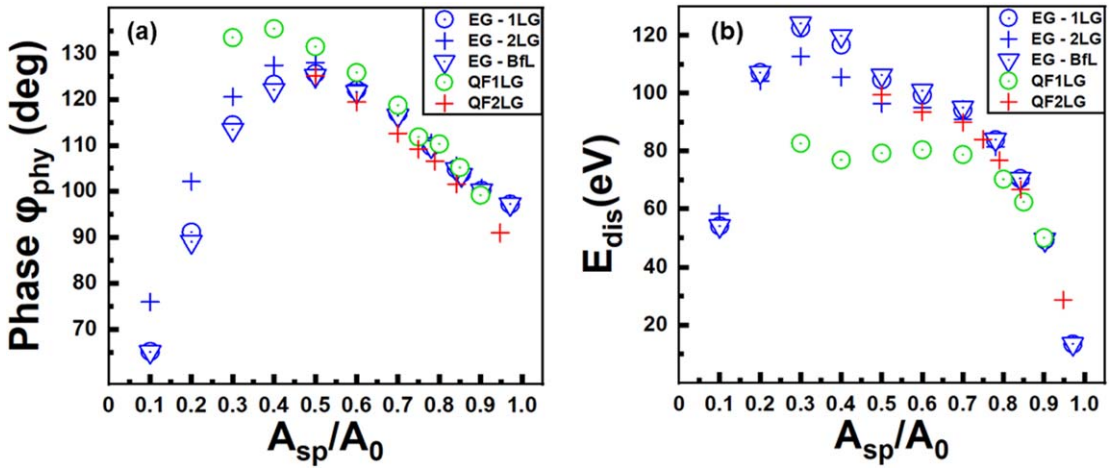


**Figure 4.** (a) Phase shift angle ($\varphi_{phy}$) variation as a function of the amplitude ratio $A_{sp}/A_0$ for the three samples measured in the experiment, namely epitaxial graphene (EG) on SiC (and respective domains of different thickness BfL, 1LG, 2LG—blue points), quasi free standing monolayer (QF1LG—green points) and quasi free standing bilayer (QF2LG—red points). Experimental conditions are the same as the experiment reported in figure 3. (b) Tip-surface energy dissipation ($E_{dis}$) as a function of the amplitude ratio $A_{sp}/A_0$, corresponding to phase angle values extracted from (a) and converted using equation (1).

probably due to an abrupt transition to the contact regime and suggest a lower surface stiffness for these samples compared to EG.

## Conclusion

In summary, we present a thorough study of the application of phase imaging to the analysis of the energy dissipation mechanisms in EG. In particular we study the different responses and interactions of the EG film to the tip oscillating over its surface. We explore the different mechanisms underlying the energy dissipative processes responsible for the emerging of the phase contrast in EG domains of different atomic thickness, and studied how they evolve in different imaging and environmental conditions, and oscillation regimes. We also sort out the effect and influence of different interaction forces on the evolution of the phase angle values. Finally, a comparison with the phase values extracted from quasi free standing graphene samples (both single layer and bilayer quasi free standing graphene) allows us to understand the influence of the SiC-carbon interface in the tip-surface interactions and dissipative processes.

Other experiments have been carried out on the same EG sample, varying different experimental parameters including $A_0$ and AFM tip, but the complex dependence of the phase shift on these and numerous other parameters and their combinations, makes it intrinsically complicated to be able to consistently control the tip-surface interactions and reproduce the data. The dependence of phase contrast on the aforementioned parameters is out of the descriptive intent of this paper. The inherent reproducibility issue is what prevents from using phase imaging as a quantitative method, and in particular, as an independent technique for assessing the exact number of atomic graphene layers.

## Acknowledgments

The Authors acknowledge the support from the Office of Basic Energy Sciences of the US Department of Energy (grant no. DE-SC0018924).

## ORCID iDs

Francesco Lavini https://orcid.org/0000-0002-5722-3040
Filippo Cellini https://orcid.org/0000-0003-1879-9634
Martin Rejhon https://orcid.org/0000-0001-7775-487X
Elisa Riedo https://orcid.org/0000-0002-2423-8801

## References


[1] Berger C *et al* 2006 Electronic confinement and coherence in patterned epitaxial graphene *Science* **312** 1191–6
[2] Wei Z Q *et al* 2010 Nanoscale tunable reduction of graphene oxide for graphene electronics *Science* **328** 1373–6
[3] Lin Y M *et al* 2011 Wafer-scale graphene integrated circuit *Science* **332** 1294–7
[4] Shivaraman S *et al* 2009 Free-standing epitaxial graphene *Nano Lett.* **9** 3100–5
[5] Gao Y *et al* 2018 Ultrahard carbon film from epitaxial two-layer graphene *Nat. Nanotechnol.* **13** 870-
[6] Robinson J A *et al* 2011 Contacting graphene *Appl. Phys. Lett.* **98** 053103
[7] Kusdemir E, Ozkendir D, Firat V and Celebi C 2015 Epitaxial graphene contact electrode for silicon carbide based ultraviolet photodetector *J. Phys. D: Appl. Phys.* **48** 095104
[8] de Heer W A *et al* 2011 Large area and structured epitaxial graphene produced by confinement controlled sublimation of silicon carbide *Proc. Natl Acad. Sci. USA* **108** 16900–5
[9] Panchal V, Pearce R, Yakimova R, Tzalenchuk A and Kazakova O 2013 Standardization of surface potential measurements of graphene domains *Sci. Rep.* **3** 2597
[10] Zhou S Y *et al* 2007 Substrate-induced bandgap opening in epitaxial graphene *Nat. Mater.* **6** 770–5
[11] Yakes M K *et al* 2010 Conductance anisotropy in epitaxial graphene sheets generated by substrate interactions *Nano Lett.* **10** 1559–62
[12] Cellini F, Lavini F, Berger C, de Heer W and Riedo E 2019 Layer dependence of graphene-diamene phase transition in epitaxial and exfoliated few-layer graphene using machine learning *2D Mater.* **6** 035043
[13] Lavini F *et al* 2018 Friction and work function oscillatory behavior for an even and odd number of layers in polycrystalline $MoS_2$ *Nanoscale* **10** 8304–12
[14] Kellar J A, Alaboson J M P, Wang Q H and Hersam M C 2010 Identifying and characterizing epitaxial graphene domains on partially graphitized SiC(0001) surfaces using scanning probe microscopy *Appl. Phys. Lett.* **96** 143103
[15] Barboza A P M *et al* 2018 Compression-induced modification of boron nitride layers: a conductive two-dimensiona BN compound *Acs Nano.* **12** 5866–72
[16] Garcia R, Magerle R and Perez R 2007 Nanoscale compositional mapping with gentle forces *Nat. Mater.* **6** 405–11
[17] Garcia R and Perez R 2002 Dynamic atomic force microscopy methods *Surf. Sci. Rep.* **47** 197–301
[18] Tamayo J and Garcia R 1998 Relationship between phase shift and energy dissipation in tapping-mode scanning force microscopy *Appl. Phys. Lett.* **73** 2926–8
[19] Magonov S N, Elings V and Whangbo M H 1997 Phase imaging and stiffness in tapping-mode atomic force microscopy *Surf. Sci.* **375** L385–91
[20] Garcia R, Gomez C J, Martinez N F, Patil S, Dietz C and Magerle R 2006 Identification of nanoscale dissipation processes by dynamic atomic force microscopy *Phys. Rev. Lett.* **97** 016103
[21] Xu J *et al* 2004 Direct AFM observation of crystal twisting and organization in banded spherulites of chiral poly(3-hydroxybutyrate-co-3-hydroxyhexanoate) *Macromolecules* **37** 4118–23
[22] Strbac S, Nenadovic M, Rajakovic L and Rakocevic Z 2010 Chemical surface composition of the polyethylene implanted by Ag+ ions studied by phase imaging atomic force microscopy *Appl. Surf. Sci.* **256** 3895–9
[23] Hibino H, Kageshima H and Nagase M 2010 Epitaxial few-layer graphene: towards single crystal growth *J. Phys. D: Appl. Phys.* **43** 374005
[24] Nagase M, Hibino H, Kageshima H and Yamaguchi H 2008 In-plane conductance measurement of graphene nanoislands using an integrated nanogap probe *Nanotechnology* **19** 495701
[25] Goler S *et al* 2013 Revealing the atomic structure of the buffer layer between SiC(0001) and epitaxial graphene *Carbon* **51** 249–54
[26] Bolen M L, Harrison S E, Biedermann L B and Capano M A 2009 Graphene formation mechanisms on 4H-SiC(0001) *Phys. Rev.* B **80** 115433
[27] Filleter T, Emtsev K V, Seyller T and Bennewitz R 2008 Local work function measurements of epitaxial graphene *Appl. Phys. Lett.* **93** 133117
[28] Filleter T *et al* 2009 Friction and dissipation in epitaxial graphene films *Phys. Rev. Lett.* **102** 086102
[29] Hass J, de Heer W A and Conrad E H 2008 The growth and morphology of epitaxial multilayer graphene *J Phys.: Condens Matter* **20** 323202
[30] Kunc J, Rejhon M and Hlidek P 2018 Hydrogen intercalation of epitaxial graphene and buffer layer probed by mid-infrared absorption and Raman spectroscopy *AIP Adv.* **8** 045015
[31] Tamayo J and Garcia R 1997 Effects of elastic and inelastic interactions on phase contrast images in tapping-mode scanning force microscopy *Appl. Phys. Lett.* **71** 2394–6
[32] James P J, Antognozzi M, Tamayo J, McMaster T J, Newton J M and Miles M J 2001 Interpretation of contrast in tapping mode AFM and shear force microscopy. A study of nafion *Langmuir* **17** 349–60.
[33] Lauffer P *et al* 2008 Atomic and electronic structure of few-layer graphene on SiC(0001) studied with scanning tunneling microscopy and spectroscopy *Phys. Rev.* B **77** 155426
[34] Filleter T and Bennewitz R 2010 Structural and frictional properties of graphene films on SiC(0001) studied by atomic force microscopy *Phys. Rev.* B **81** 155412
[35] Cellini F *et al* 2018 Epitaxial two-layer graphene under pressure: diamene stiffer than diamond *FlatChem.* **10** 8–13
[36] Cellini F, Gao Y and Riedo E 2019 A-Indentation for non-destructive elastic moduli measurements of supported ultra-hard ultra-thin films and nanostructures *Sci. Rep.* **9** 4075
[37] Garcia R and San Paulo A 2000 Amplitude curves and operating regimes in dynamic atomic force microscopy *Ultramicroscopy* **82** 79–83
[38] Garcia R and San Paulo A 1999 Attractive and repulsive tip-sample interaction regimes in tapping-mode atomic force microscopy *Phys. Rev.* B **60** 4961–7
[39] Gomez C J and Garcia R 2010 Determination and simulation of nanoscale energy dissipation processes in amplitude modulation AFM *Ultramicroscopy* **110** 626–33
[40] Chiou Y C *et al* 2018 Direct measurement of the magnitude of the van der Waals interaction of single and multilayer graphene *Langmuir* **34** 12335–43
[41] Rafiee J *et al* 2012 Wetting transparency of graphene *Nat. Mater.* **11** 217–22
[42] Munz M, Giusca C E, Myers-Ward R L, Gaskill D K and Kazakova O 2015 Thickness-dependent hydrophobicity of epitaxial graphene *ACS Nano* **9** 8401–11
[43] Zhou H *et al* 2012 Understanding controls on interfacial wetting at epitaxial graphene: experiment and theory *Phys. Rev.* B **85** 035406